Growth rates for fast kinematic dynamo instabilities of chaotic fluid flows†

By YUNSON DU and EDWARD OTT‡

Laboratory for Plasma Research and Department of Physics, University of Maryland, College Park, MD 20742-3511, USA

It is shown that the exponential growth rate of the fast kinematic dynamo instability can be related to the Lagrangian stretching properties of the underlying chaotic flow. In particular, a formula is obtained relating the growth rate to the finite time Lyapunov numbers of the flow and the cancellation exponent κ. (The latter quantity characterizes the extremely singular nature of the magnetic field with respect to fine-scale spatial oscillation in orientation.) The growth rate formula is illustrated and tested on two examples: an analytically soluble model, and a numerically solved spatially smooth temporally periodic flow.

1. Introduction

This paper considers the fast kinematic dynamo problem. The limit of the instability growth rate as the electrical resistivity approaches zero is shown to be given by a simple general formula involving the finite-time Lyapunov numbers of the underlying chaotic flow.

The kinematic magnetic dynamo problem can be stated as follows: Will a small seed magnetic field in an unmagnetized electrically conducting fluid be amplified exponentially in time by the flow? Combining Ampere's law, Faraday's law, and Ohm's law for the flowing incompressible fluid, this linear instability problem leads to the following equation for the magnetic field B:

$$\frac{\partial B}{\partial t} + v \cdot \nabla B = B \cdot \nabla v + \frac{1}{R_m} \nabla^2 B, \tag{1}$$

where R_m is the magnetic Reynolds number (i.e. the normalized electrical conductivity of the fluid), and the velocity v is presumed given and incompressible, $\nabla \cdot v = 0$. The dynamo is said to be 'fast' if exponential growth persists in the limit of infinitely large R_m (Zel'dovich & Ruzmaikin 1980). That is, $\gamma_* > 0$, where

$$\gamma_* = \varlimsup_{R_m \to \infty} \gamma(R_m), \tag{2}$$

and $\gamma(R_m)$ is the growth rate of the fastest growing mode at magnetic Reynolds number R_m. Fast dynamos are thought to be relevant to explaining the presence of magnetic fields in astrophysical objects, since these objects typically have very large magnetic Reynolds number (e.g. $R_m > 10^8$ on the surface of the Sun).

† With an Appendix by B. J. Bayly and A. Rado.
‡ And Department of Electrical Engineering.

It has been argued that fast dynamo action in a flow is connected with the nonlinear dynamics of the Lagrangian trajectory equation for points in the fluid,

$$\frac{dx}{dt} = v(x, t). \tag{3}$$

In particular, fast dynamo action of a smooth flow is expected (Arnol'd *et al.* 1981; Bayly 1986; Bayly & Childress 1988; Finn & Ott 1988; Finn *et al.* 1991; Galloway & Frisch 1986; Vishik 1989) only if this equation has chaotic solutions in the sense that, in a positive volume of space, there is exponential divergence of infinitesimally displaced initial conditions. We call this situation *Lagrangian chaos*. Finn & Ott (1990) conjectured that the limiting growth rate γ_* given by (2) is the same as the exponential rate of flux growth through typical surfaces calculated from the 'ideal' (i.e. infinite conductivity) version of (1),

$$\frac{\partial B}{\partial t} + v \cdot \nabla B = B \cdot \nabla v, \tag{4}$$

which results from the omission of the term $\nabla^2 B / R_m$. This is a considerable simplification because (4) can be written as an ordinary differential equation,

$$\frac{dB}{dt} = B \cdot \nabla v, \tag{5a}$$

following the Lagrangian trajectory $x(t)$ of a fluid particle. Alternatively (5a) can be written as

$$\frac{dB}{dt} = \mathcal{M} \cdot B, \tag{5b}$$

where the 3×3 matrix $\mathcal{M}$ is given by $\mathcal{M} = (\nabla v)^+$, where $+$ denotes the transpose. Consideration of two orbits of (3) initially displaced by an infinitesimal $\delta x(0)$ leads to an equation for the time evolution of the displacement δx,

$$\frac{d\delta x}{dt} = \delta x \cdot \nabla v = \mathcal{M} \cdot \delta x, \tag{6}$$

which is the same as (5) with B replaced by δx. Thus, in the infinite-conductivity case, B and δx evolve in the same way. Note that the replacement of (1) by (4) is not trivial, since, as R_m becomes large, B varies more and more rapidly in space, and $\nabla^2 B / R_m$ is thus not necessarily small; this is why the prescription of Finn & Ott (1990) remains a conjecture. In this paper we attempt to calculate the limiting growth rate γ_* purely from general stretching properties of the Lagrangian chaotic flow $v(x, t)$. Thus, as in the conjecture of Finn & Ott (1990), the result is in terms of quantities calculable solely from the dissipationless equation for B, (5) (equivalently, (6)). We obtain a formula ((23) of §3) giving γ_* in terms of the finite-time Lyapunov numbers of the flow and the cancellation exponent κ. (The latter quantity characterizes the extreme tendency of high-R_m dynamo magnetic fields to oscillate in sign on a very fine spatial scale (Du & Ott 1993; Ott *et al.* 1992).) Related results are those of Aurell & Gilbert (1992), who calculate γ_* in terms of unstable periodic orbits in the flow, and of Finn & Ott (1990), who argue that the logarithm of the average rate of stretching (where the average is done appropriately) is an upper bound for γ_*. In fact, our result in the present paper

reduces to the upper bound of Finn & Ott (1990) in the absence of cancellation effects ($\kappa = 0$), and is smaller than the upper bound when cancellation is present ($\kappa > 0$).

The formula we obtain for γ_* is interesting in that it provides a connection to the ergodic stretching properties of the flow. In addition, however, the numerical results of §5 also show that it offers a potential computational advantage. In particular, the growth rate formula appears to be much easier to compute numerically and to converge quicker than a straightforward computation of the flux growth through a surface (Finn & Ott 1990).

In this paper we take the underlying unperturbed flow $v(x, t)$ to be such as to yield Lagrangian chaos, meaning that (6) has an exponentially growing solution for typical fluid trajectories $x(t)$ in a volume of space. The actual time dependence of v can be steady ($v = v(x)$), periodic ($v(x, t) = v(x, t + T)$ where T is the period), or be more complicated. In the last case, the fluid equations yielding the unperturbed $v(x, t)$ may be chaotic in a second sense, namely that the time dependence of $v(x, t)$ at *fixed* x may be chaotic. We refer to this as *temporal chaos* of the unperturbed solution, and we emphasize its distinction from Lagrangian chaos.

For steady and time-periodic flows, the Lagrangian orbits can be either chaotic or non-chaotic, and when an orbit $x(t)$ is non-chaotic, its time dependence is quasi-periodic (corresponding to a KAM torus). In cases where there are chaotic regions amidst KAM tori, the considerations of our paper should be understood to apply to a single chaotic ergodic region of the flow. In the examples we treat in §§4 and 5, we use particular time-periodic flows v. For these flows there is Lagrangian chaos over essentially the whole space. We believe, however, that the results obtained are indicative of what happens in general, including *steady* flows that have ergodic regions of Lagrangian chaos, as well as temporally chaotic flows.

The organization of this paper is as follows. Section 2 reviews the concept of the cancellation exponent (Du & Ott 1993; Ott *et al.* 1992) which plays an essential role in the subsequent analysis. Section 3 develops the growth rate formula for the fast dynamo problem. The growth rate formula is not obtained rigorously, and so it is useful to test it in examples. This is done in §§4 and 5. Section 4 treats an analytically soluble case of the 'stretch–fold–slide' type (a variant of the 'stretch–fold–shear' dynamo introduced by Bayly & Childress 1988 and Soward 1987). The example of §5 is a numerically solved spatially smooth temporally periodic flow (Finn & Ott 1988; Du & Ott 1993). For another numerical confirmation see the addendum by Bayly & Rado that appears as Appendix B.

2. Cancellation exponent

Consider, for definiteness, the case of a steady flow, $v = v(x)$. In this case (1) yields an eigenvalue problem,

$$s_j b_j(x) + v \cdot \nabla b_j(x) = b_j(x) \cdot \nabla v + \frac{1}{R_m} \nabla^2 b_j(x), \qquad (7)$$

for a magnetic field with space–time variation $B(x, t) = e^{s_j t} b_j(x)$, where s_j is the (complex) eigenvalue corresponding to the jth eigenfunction $b_j(x)$. For a typical initial condition, $B(x, 0)$, all eigenfunctions are excited. However, after a sufficient time, $B(x, t)$ will be dominated by the eigenfunction with the largest growth rate (i.e. largest $\text{Re}(s_j)$). Theory and numerical results show that the corresponding eigenfunction $b_j(x)$ varies on fine scale for large R_m. In fact, balancing the last term in (1) with the
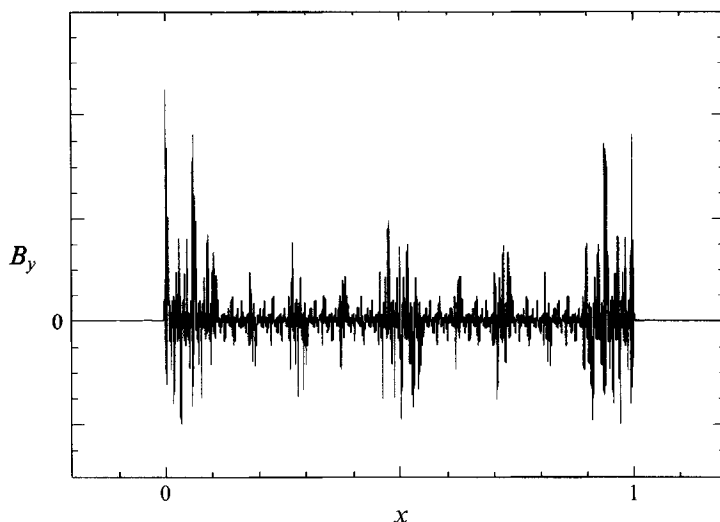
FIGURE 1. B_y versus x for the model of (Ott *et al.* 1992; Du & Ott 1993) with $R_m = 10^7$.

other terms in the equation, one finds that the typical lengthscale for variation of the magnetic field is (Moffatt & Proctor 1985)

$$\epsilon_* = L_0/R_m^{\frac{1}{2}}, \tag{8}$$

where L_0 is the lengthscale of the unperturbed flow v. Thus, as R_m is increased, $b_j(x)$ varies on finer and finer scale. Figure 1 (from Du & Ott 1993) shows the magnetic field in the y-direction as a function of the linear coordinate x for $R_m = 10^7$ after the field has settled into its large-time asymptotic form. (The system resulting in figure 1 is a simple baker's map dynamo model on the interval $0 \leqslant x \leqslant 1$ which we shall not describe here.) The point is that the magnetic field in figure 1 exhibits extremely rapid oscillations from positive to negative values, and this situation becomes more and more extreme as R_m is increased.

In order to characterize this type of singular behaviour, a 'cancellation exponent' κ was introduced in Du & Ott (1993) (see also Ott *et al.* 1992). As an example, consider the situation in figure 1, and divide the x-axis into equal-length intervals of size ϵ. We then introduce the quantity,

$$\chi(\epsilon) = \sum_i \left| \int_i B_y(x, t) \, dx \right| \bigg/ \left| \int_0^1 B_y(x, t) \, dx \right|, \tag{9}$$

where $\int_i, \ldots, dx$ denotes the integral over the ith interval of length ϵ, and t is large enough that the x-dependence of B_y has reached its final form in which there are variations on the scale given by (8). Figure 2 shows a plot of $\ln \chi(\epsilon)$ versus $\ln(1/\epsilon)$. The data are well fit by a straight line for $\epsilon > \epsilon_* \sim 1/R_m^{\frac{1}{2}}$. (The deviation from the straight line at large $\ln(1/\epsilon)$ is numerically observed to occur at smaller ϵ if R_m is increased). Thus in the scaling range, $1 \gg \epsilon \gtrsim \epsilon_*$, we have

$$\chi(\epsilon) \sim 1/\epsilon^\kappa,$$

where the exponent κ is the slope of the straight line in figure 2. We call κ the cancellation exponent. It is a quantitative characterization of the very rapid oscillations in the sign of B_y. For example, if B_y were always positive, then the numerator and denominator of (9) would be the same, so that $\chi(\epsilon) = 1$, and $\kappa = 0$ (no cancellation).
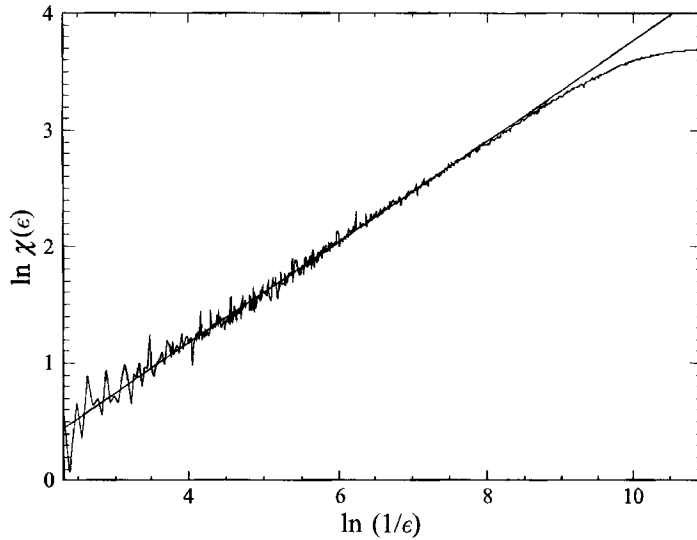
FIGURE 2. $\ln \chi$ versus $\ln(1/\epsilon)$ for the same model (Ott *et al.* 1992; Du & Ott 1993) as was used for figure 1 with $R_m = 10^{10}$, $\kappa = 0.43$.

Increase of $\chi(\epsilon)$ with decreasing ϵ (which is necessary to obtain $\kappa > 0$) occurs only because cancellations between positive and negative B_y in the sum $\Sigma_i |\int_i B_y \, dx|$ are reduced for smaller ϵ.

Note from figure 2 that for $\epsilon \lesssim \epsilon_*$, the quantity $\chi(\epsilon)$ becomes constant. This is because B_y is locally approximately constant over distances less than ϵ_*. Hence, for large t and $\epsilon \lesssim \epsilon_*$, we have

$$\sum_i \left| \int_i B_y \, dx \right| \approx \int_0^1 |B_y| \, dx, \quad \text{while} \quad \sum_i \left| \int_i B_y \, dx \right| \approx (1/\epsilon^\kappa) \left| \int_0^1 B_y \, dx \right|.$$

Thus setting $\epsilon = \epsilon_*$, we conclude that

$$\int_0^1 |B_y| \, dx \Big/ \left| \int_0^1 B_y \, dx \right| \approx 1/\epsilon_*^\kappa. \tag{10}$$

The above considerations, illustrated for the variation of B_y along a line, readily generalize to surface and volume integrals (Du & Ott 1993). The case of interest here is a volume, for which (9) is replaced by

$$\chi(\epsilon) = \sum_i \left| \int_i B(x, t) \, d^3 x \right| \Big/ \left| \int_V B(x, t) \, d^3 x \right|, \tag{11}$$

where now i denotes a cube from an ϵ-grid which covers the active dynamo volume V (we assume that the denominator in (11) is not zero), and (10) is replaced by

$$\int_V |B(x, t)| \, d^3 x \Big/ \left| \int_V B(x, t) \, d^3 x \right| \approx (L_0/\epsilon_*)^\kappa. \tag{12}$$

So far we have been considering the case of large but finite magnetic Reynolds number. In fact, the cancellation exponent can be computed directly from the infinite-conductivity equation, (4). This represents an important simplification because now one only need integrate ordinary differential equations, (5). In this case the solution of

(4) for a smooth initial condition continues to develop variation on finer and finer scale as time increases, and this process continues forever. On inserting a large- but finite-time solution of (4) for B in

$$\tilde{\chi}(\epsilon) = \sum_i \left| \int_i B(x, t) \, \mathrm{d}^3 x \right| \Big/ \left| \int_V B(x, t) \, \mathrm{d}^3 x \right|, \tag{13}$$

a result similar to figure 2 still applies, and the resulting slope κ in the scaling range is the same (Du & Ott 1993) as would be obtained for the same flow with a large finite R_m and t large enough that the final spatial form determined by (8) has been attained. The difference is that now the small-ϵ cut off of the scaling range depends on how large t is, and it decreases exponentially to zero with increasing t. The equality of the two results for κ is shown in Du & Ott (1993) and is reasonable on the basis that the effect of resistivity is diffusive (the term $R_m^{-1} \nabla^2 B$ in (1)) and thus manifests itself as a smoothing of the magnetic field on the scale ϵ_* of (8). Such smoothing makes only a small change in $| \int_t B(x, t) \, \mathrm{d}^3 x |$ if the dimension of the cube ϵ is large compared to ϵ_*. Hence, the scalings of $\chi(\epsilon)$ and of $\tilde{\chi}(\epsilon)$ are expected to be the same for $\epsilon > \epsilon_*$. (See Du & Ott 1993 for numerical tests and further discussion.) (In 13) note that we have placed a tilde over χ to signify that the calculation is done using the magnetic field obtained from the infinite conductivity equation, as opposed to (11) where a large finite R_m is used.)

3. Growth rate formula

Assume that enough time has passed so that the magnetic field in a dynamo with large but finite magnetic Reynolds number ($R_m \gg 1$) has evolved to the time-asymptotic state where field variations occur on the lengthscale $L_0/R_m^{\frac{1}{2}}$ (equation (8)). Now imagine that we divide the dynamo region into a grid of cubes of unit size δ, one of which (cube j) is shown in figure 3(a). Let $x = x_{0j}$ denote the point at the centre of the cube, and let the cube be small enough that the action of the flow over a time interval t is to deform the cube in accord with (6), the linear approximation for small deviations from an orbit. Let $M(x_{0j}, t, \tau)$, obtained from solving (6), be the matrix relating δx at time τ and location $x = x_{0j}$ to δx at time $\tau + t$ and location $x = x_j$,

$$\delta x_j(t) = M(x_{0j}, t, \tau) \cdot \delta x_{0j}. \tag{14}$$

As a result of the flow, the cube is deformed into a long thin flat parallelepiped (figure 3(b) of dimensions (length, width, thickness) of the order of $L_{j1} \delta \times L_{j2} \delta \times L_{j3} \delta$, where $L_{j1,2,3}$ are the magnitudes of the three eigenvalues of $M(x_{0j}, t, \tau)$, and we choose the subscripts 1, 2 and 3 so that

$$L_{j1} \geqslant L_{j2} \geqslant L_{j3}.$$

Because the flow is incompressible, $L_{j1} L_{j2} L_{3j} = 1$. Since the flow is taken to be chaotic, we assume $L_{j1} > 1$, and, by incompressibility, we must then also have $L_{j3} < 1$. It suffices to think of the parallelepiped that J maps to as a rectangular slab (figure 3c). To see that this is so, we note that we will only need order of magnitude estimates of $\int |B| \, \mathrm{d}V$ over J and over the parallelepiped to which J maps. We also note that, for typical flows and typical points x_{0j}, the angles between the eigenvectors of the matrix $M(x_{0j}, t, \tau)$ are order one. Thus our required estimates can be obtained by replacing J by a parallelepiped J' whose centre is at x_{0j} and whose edges are of length δ and are parallel to the eigendirections of $M(x_{0j}, t, \tau)$. Mapping J' forward by t, we obtain another long thin flat parallelepiped (overlapping that in figure 3c). The point is that
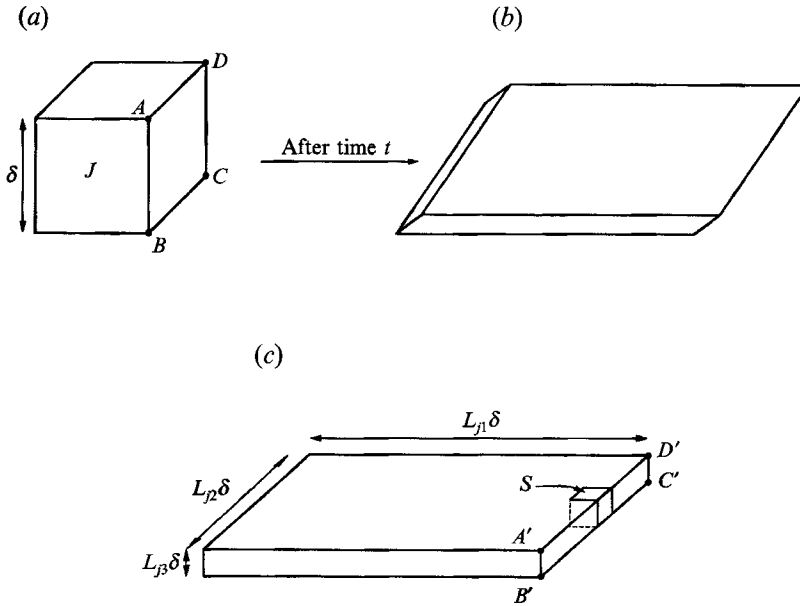
FIGURE 3. (*a*) Cube of edge length δ. (*b*) Deformation of cube in (*a*). (*c*) Rectangular slab idealization of (*b*).

the angles between the edges of this parallelepiped will also be order one, and making the edges perpendicular will thus not significantly alter our estimates. We are interested in large t, so that $L_{j1} \gg L_{j3}$. On the other hand, we cannot let t be too large since we will also require that

$$L_{j1} \delta \ll L_0, \qquad L_{j3} \delta \gg L_0/R_m^{\frac{1}{2}}. \tag{15}$$

For a large fixed value of t and sufficiently large R_m, we can choose a δ such that these inequalities hold. The first inequality is necessary so that the linear approximation given by the matrix $M(x_{0j}, t, \tau)$ is valid in cube j.

Now imagine that we divide the slab in figure 3(*c*) into small cubes of edge length $L_{j3} \delta$. The number of such small cubes in the slab will be of the order of

$$N_j = \frac{L_{j1} L_{j2}}{L_{j3} L_{j3}} = L_{j3}^{-3}, \tag{16}$$

where the second equality follows from the incompressibility condition.

To proceed, it is necessary, at this point, to make an additional assumption which restricts the type of chaotic flows that we consider. In particular, we shall assume here that the magnetic field has local sheet-like structure. By sheet-like structure we mean that the magnetic field is slowly varying on locally parallel surfaces (sheets), across which the variation is very rapid, and, for scales larger than $L_0/R_m^{\frac{1}{2}}$, the field effectively concentrates on a fractal set of these sheets (Du & Ott 1993). This is so for the important case of steady flows. More generally, as shown in Du & Ott (1993), for there to be sheet-like structure it is necessary that the flow be non-contracting in two directions, i.e. in addition to the condition $L_{j1} > 1$, implied by the assumed chaos of the flow, we also require $L_{j2} \geqslant 1$. To see why sheet-like structure is implied for the case of two expanding directions, $L_{j1,2} > 1 > L_{j3}$, we note that under this condition, at a point x there is a two-dimensional unstable manifold (the sheet) through x. Taking a point

x' on the sheet through x and using (3) to evolve the orbits through x and x' backward to time zero, the two backward orbits approach each other exponentially. Thus, if the points x and x' are close, then the orbits leading to them from time zero were always close. Hence integration of (5) yields nearly the same B at the two points x and x'. On the other hand, if x' were chosen near x, but on a different sheet, then the backward orbits through x and x' would diverge exponentially. If, by time zero, the two orbits have separated by a distance of the order of L_0, then the values of B at x and x', obtained by integrating (5), would be very different. Hence, for large time, B varies wildly across the sheets. (When there is contraction in two dimensions, $L_{j2} < 1$, the field is smooth only in the one expanding direction, and is fractal in the two directions transverse to it (Du & Ott 1993); we then say that the field structure is rope-like.) In practice, given an unperturbed flow v, it is not hard to numerically test whether the assumption of locally sheet-like magnetic field structure applies (see §5). The important point is that, in the case of locally sheet-like structure, the fields in all of the small cubes that we have divided the slab in figure 3(c) into are roughly the same; for example this is certainly so if the sheets are parallel to the plane determined by the largest area face of the slab in figure 3(c). Indeed, stretching in the directions corresponding to L_{j1} and L_{j2} tends to align this plane with the sheets.

If there were no resistive diffusion (the term $\nabla^2 B/R_m$ in (1)), the magnetic field following a point initially in the cube of figure 3(a) would increase in proportion to the net stretching of a field line element (i.e. by a factor of order L_{j1}), and the spatial scale for variation of the field would decrease by a factor of order L_{j3}. However, resistive diffusion prevents variations on scales smaller than $L_0/R_m^{\frac{1}{2}}$ (equation (8)). Thus, in the presence of small diffusion, the contraction of the cube along the L_{j3} direction does not create scale variations finer than $L_0/R_m^{\frac{1}{2}}$.

Denote by J the original cube (figure 3a) and by S one of the small cubes of edge length $L_{j3}\delta$; see figure 3(c). If we magnify S by a factor L_{j3}^{-1}, then the resulting magnetic field variations in J will differ from those in S in that the fine-scale field variations in J are cut off at $\epsilon_* \sim L_0/R_m^{\frac{1}{2}}$, while those in the magnified-S cube are cut off at the larger (magnified) scale $\epsilon_{**} \sim L_{j3}^{-1}\epsilon_* \sim L_{j3}^{-1}L_0/R_m^{\frac{1}{2}}$. (The second inequality in (15) says that the scale ϵ_{**} is small compared to the edge length δ of the magnified cube.) Hence by (12) we have

$$\int_S |B|\,\mathrm{d}^3x \bigg/ \left|\int_S B\,\mathrm{d}^3x\right| \approx (\epsilon_{**}/L_0)^{-\kappa},$$

and

$$\int_J |B|\,\mathrm{d}^3x \bigg/ \left|\int_J B\,\mathrm{d}^3x\right| \approx (\epsilon_*/L_0)^{-\kappa}.$$

Thus

$$\frac{\displaystyle\int_S |B|\,\mathrm{d}^3x}{\left|\displaystyle\int_S B\,\mathrm{d}^3x\right|} \approx (L_{j3})^{\kappa}\frac{\displaystyle\int_J |B|\,\mathrm{d}^3x}{\left|\displaystyle\int_J B\,\mathrm{d}^3x\right|}. \tag{17}$$

Now consider the area $ABCD$ shown in figure 3(a). During the time t this area is carried to $A'B'C'D'$ as shown in figure 3(c). Since $L_{j3}\delta \gg L_0/R_m^{\frac{1}{2}}$, the magnetic flux is effectively frozen in as the area convects so that the fluxes through $ABCD$ and $A'B'C'D'$ are approximately equal. Thus we have

$$\left|\int_S B\,\mathrm{d}^3x\right| \approx (L_{j3}/L_{j2})\,L_{j3}\times\left|\int_J B\,\mathrm{d}^3x\right|.$$

Using (16) and the incompressibility condition, $L_{j1} L_{j2} L_{j3} = 1$, this becomes

$$N_j \left| \int_S \boldsymbol{B} \, \mathrm{d}^3 x \right| \approx L_{j1} \left| \left| \int_J \boldsymbol{B} \, \mathrm{d}^3 x \right| \right|. \tag{18}$$

The factor L_{j1} on the right-hand side of (18) results simply from the fact that, in the absence of electrical resistivity, $\boldsymbol{B}$ obeys the same equation as δx (see (5) and (6)). Thus

$$\boldsymbol{B}|_{\text{in slab, at time } t+\tau} \approx \boldsymbol{M}(x_{0j}, t, \tau) \cdot \boldsymbol{B}|_{\text{in } J, \text{ at time } \tau}, \tag{19}$$

and $\boldsymbol{B}$ grows by the factor roughly L_{j1} (the magnitude of the largest eigenvalue of $\boldsymbol{M}$). Combining (17) and (18), we have

$$L_{j1} L_{j3}^\kappa \int_J |\boldsymbol{B}| \, \mathrm{d}^3 x \approx N_j \int_S |\boldsymbol{B}| \, \mathrm{d}^3 x. \tag{20}$$

Summing over all cubes j yields

$$\sum_j \left[(L_{j1} L_{j3}^\kappa) \int_{J_j} |\boldsymbol{B}| \, \mathrm{d}^3 x \right] \approx \left[\int_V |\boldsymbol{B}| \, \mathrm{d}^3 x \right]_{\text{time } t+\tau}, \tag{21}$$

where V denotes the entire ergodic dynamo region. The quantity summed over j on the left-hand side of (21) consists of two factors: one factor, $L_{j1} L_{j3}^\kappa$, is determined by the orbit during the time interval t; the other factor, $\int_{J_j} |\boldsymbol{B}| \, \mathrm{d}^3 x$, is determined by the evolution prior to the time interval t. By the assumed chaotic nature of the orbits, the distant future and the distant past (distant in terms of many Lyapunov times) are effectively uncorrelated. Hence

$$\sum_j (L_{j1} L_{j3}^\kappa) \int_{J_j} |\boldsymbol{B}| \, \mathrm{d}^3 x \approx \langle L_1(x, t) L_3^\kappa(x, t) \rangle \sum_j \int_{J_j} \boldsymbol{B} \, \mathrm{d}^3 x$$

$$= \langle L_1(x, t) L_3^\kappa(x, t) \rangle \left[\int_V |\boldsymbol{B}| \, \mathrm{d}^3 x \right]_{\text{time } \tau}, \tag{22}$$

where $L_i(x, t)$ are the magnitudes of the three eigenvalues ($i = 1, 2, 3$) of $\boldsymbol{M}(x, t, \tau)$ and $\langle \ldots \rangle$ indicates an average over x in the volume V. From (21) and (22)

$$\left[\int_V |\boldsymbol{B}| \, \mathrm{d}^3 x \right]_{\text{time } t+\tau} \approx \langle L_1 L_3^\kappa \rangle \left[\int_V |\boldsymbol{B}| \, \mathrm{d}^3 x \right]_{\text{time } \tau}. \tag{23}$$

We now assume that during the time interval t the magnetic field grows roughly as $\exp(\gamma_* t)$ (cf. (2)). (This neglects other non-exponential time dependences of the magnetic field, such as superposed sinusoidal dependences (appropriate for steady or time-periodic flows) or a more complicated time dependence when v is temporally chaotic.) Equation (23) thus leads to the *main result of this paper*,

$$\gamma_* = \lim_{t \to \infty} \frac{1}{t} \ln \langle L_1 L_3^\kappa \rangle, \tag{24}$$

which relates an infinite time limit of an average of the finite-time Lyapunov numbers, L_1 and L_3, and the cancelation exponent, κ, to the dynamo growth rate, γ_*. Note that cancellation ($\kappa > 0$) decreases γ_* from the upper bound conjectured in Finn & Ott (1990),

$$\gamma_* \leqslant \lim_{t \to \infty} \frac{1}{t} \ln \langle L_1 \rangle. \tag{25}$$

Under certain conditions (Yomdin 1987) the right-hand side of (25) may be identified with the topological entropy of the flow.

In order to numerically utilize (24), one can proceed as follows. First sheet-like structure must be confirmed. A rough way of doing this is to calculate the Lyapunov exponents in the ergodic dynamo region; if two of them are non-negative, then that is a good indication that the structure will be sheet-like. Another method is to solve (5) numerically to make contour plots on a plane cutting the dynamo region of the component of B normal to the plane (cf. figure 8 of §5 and Du & Ott 1993). As time increases, one can see, in such plots, that the regions of large magnetic field tend either (Du & Ott 1993) to locally parallel curves (the intersections of the sheets with the plane) or many ever-decreasing-in-diameter blobs (the intersections of the ropes with the plane). (This type of computation is described further in §5.) If sheet-like structure is confirmed, the next step is to calculate the cancellation exponent. Since the structure is sheet-like, this can be done using a line segment cutting the sheets (rather than a volume, as in (11)). After choosing a line segment in the dynamo region, a component of B normal to the line is computed (again using (5)) at a large number of evenly spaced points along the line at a time sufficiently large that B varies on a very fine scale. The cancellation exponent is then computed as the slope of a plot of $\ln \tilde{\chi}(\epsilon)$ (see (13)) versus $\ln (1/\epsilon)$ in the scaling range. Next we compute $\langle L_1 L_3^\kappa \rangle$ and plot $\ln \langle L_1 L_3^\kappa \rangle$ versus t. The estimated value of the growth rate γ_* is then the slope of this plot. To compute $\langle L_1 L_3^\kappa \rangle$, we proceed as follows. We first sprinkle many initial conditions uniformly in the ergodic dynamo region V. Then for each initial condition x, we compute L_1 by choosing an arbitrary initial δx_0 and integrating $\mathrm{d}\delta x/\mathrm{d}t = \mathcal{M} \cdot \delta x$ forward, along the trajectory from x, for time t. Since L_1 is the magnitude of the largest eigenvalue of $M(x, t, \tau)$, we have that, for a typical choice of δx,

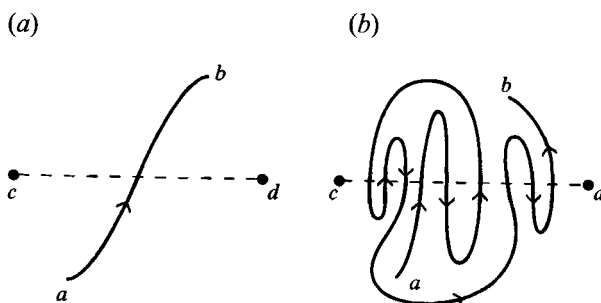$$L_1 \approx \frac{1}{t} \ln \left(\frac{|\delta x(t)|}{|\delta x_0|} \right). \tag{26}$$

Next, we obtain L_3 at x by choosing an arbitrary 'final' δx_t at x and integrating $\mathrm{d}\delta x/\mathrm{d}t = \mathcal{M} \cdot \delta x$ backward to $x(0)$ to obtain $\delta x(0)$. Since $1/L_3$ is the magnitude of the largest eigenvalue of $\mathcal{M}^{-1}$ we have,

$$L_3 \approx \frac{1}{t} \ln \left(\frac{|\delta x(0)|}{|\delta x_t|} \right). \tag{27}$$

We then form the quantity $L_1 L_3^\kappa$ and average its value over all the initial conditions. Care must be taken in doing these computations, because the requirement of having good statistics for the average typically becomes more difficult to satisfy at later times (thus requiring the use of more initial conditions). In the example of §4, we use both (24), and a direct computation of the diffusionless exponential flux growth rate through a line segment to estimate γ_*. The two computations agree to within the accuracy obtained, but the computation based on (24) is much less demanding and also converges more rapidly.

Remark. It is well-known that fast dynamo growth is inherently a three-dimensional process (Zel'dovich's antidynamo theorem). For example, in a purely two-dimensional situation where B and v depend only on x and y and lie in the (x, y)-plane, no dynamo growth is possible. In the context of our growth rate formula, (24), this is reflected by the fact that cancellation is essentially perfect in two dimensions; $\kappa = \infty$ (see the remark following (46b)), which, from (24), yields no growth. As shown in figure 4, perfect cancellation in this case is due to the topological constraint that magnetic field

(a)   (b)

FIGURE 4. Flux tube *ab* in (a) evolves under a chaotic flow to (b).

lines do not cross as the situation evolves, and this applies whether or not the two-dimensional flow is Lagrangian chaotic. Figure 4 shows a single flux tube with its ends anchored at the points *a* and *b*. At $t = 0$ (figure 4*a*) the flux tube crosses the line *cd*, creating one unit of upward flux. As time goes on the flux tube is stretched and contorted. At some later time (figure 4*b*) the net upward flux through *cd* can only be either $+1$, -1 or 0 (in units of the flux at $t = 0$) because upward and downward crossings of *cd* by the flux tube precisely alternate.

Remark. Since $L_3 \leqslant 1/L_1$ for sheet-like magnetic field structure, we see that (24) can yield exponential growth only if $\kappa < 1$. See Appendix A for a discussion of the case $\kappa > 1$.

4. Stretch–fold–slide dynamo

4.1. *The model*

Bayly & Childress (1988) consider time-periodic flows that are independent of the axial coordinate z and that, in each time period, consist of two phases. In the first phase $v_z = 0$, so that fluid particle displacements are purely in the x- and y-directions. If at the beginning of the nth period a fluid element has coordinates x_n and y_n, its x and y-coordinates after the first phase of motion are displaced according to a two-dimensional map,

$$(x_{n+1}, y_{n+1}) = (F_1(x_n, y_n), F_2(x_n, y_n)). \tag{28}$$

During the second phase $v_z \neq 0$, but $v_x = v_y = 0$, so that the fluid particle displacement $\Delta(x, y)$ is purely in the z-direction,

$$z_{n+1} = z_n + \Delta(x_n, y_n). \tag{29}$$

In a case, such as that above, where $v(x, t)$ is time periodic with period T,

$$(v(x, t) = v(x, t + T)),$$

the solution of the trajectory equation, $dx/dt = v(x, t)$, yields a map giving x at time $t = (n+1)T$ in terms of x at time $t = nT$,

$$x_{n+1} = M(x_n),$$

where $x_n = (x_n, y_n, z_n)$. Let $B_n(x)$ denote the magnetic field at time $t = nT$. Since B evolves in the same way as δx in the infinite-conductivity case ((5*a*) and (6) are the same), the evolution of B_n is governed by the Jacobian matrix $DM(x)$ of the map. That is

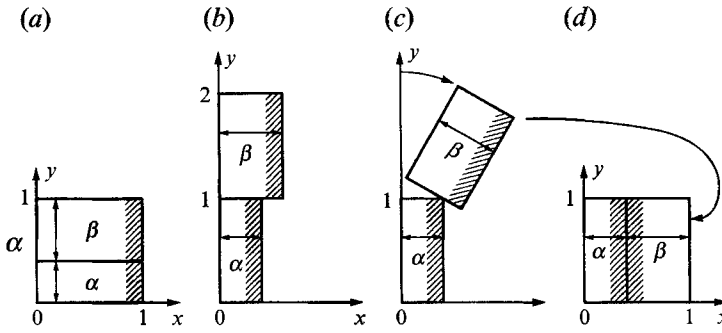$$B_{n+1}(x) = DM(M^{-1}(x)) \cdot B_n(M^{-1}(x)). \tag{30}$$

FIGURE 5. Action of the map (31) on the unit square, $(0,0) \leqslant (x,y) \leqslant (1,1)$. $(a) \rightarrow (b)$: incompressible stretch; $(b) \rightarrow (c) \rightarrow (d)$: fold.

We now specialize to a particular form for the two-dimensional map (28) (Finn & Ott 1988),

$$x_{n+1} = \begin{cases} \alpha x_n & \text{for } y_n < \alpha, \\ \beta(1-x_n)+\alpha & \text{for } y_n \geqslant \alpha, \end{cases} \tag{31a}$$

$$y_{n+1} = \begin{cases} y_n/\alpha & \text{for } y_n < \alpha, \\ (1-y_n)/\beta & \text{for } y_n \geqslant \alpha, \end{cases} \tag{31b}$$

where $\alpha + \beta = 1$. This map is an incompressible version of the 'generalized baker's map' (Farmer, Ott & Yorke 1983). Its action on the unit square is illustrated in figure 5. In addition, to further facilitate the analysis, we take v_z during the shear phase to be $v_z = 0$ for $x < \alpha$ and $v_z = v_{z0}$ for $x > \alpha$, where $v_{z0}(t)$ is spatially constant in $x > \alpha$. Thus, Δ appearing in (29) is likewise zero in $x < \alpha$ and a constant, call it Δ_0, in $x > \alpha$. That is, we *slide* the region $x > \alpha$ forward by the distance Δ_0. Let the magnetic field at the end of the nth step be independent of y and of the form

$$B = \text{Re}\{B_n(x)\exp(\mathrm{i}kz)\,y_0\}, \tag{32}$$

where the exponential z-dependence corresponds to the assumed homogeneity of the flow in z. Equation (30) then yields

$$B_{n+1}(x) = \begin{cases} \alpha^{-1}B_n(x/\alpha) & \text{for } x < \alpha, \\ \beta^{-1}B_n[(1-x)/\beta]\,\mathrm{e}^{\mathrm{i}\theta} & \text{for } x > \alpha, \end{cases} \tag{33a}$$

where $\theta = k\Delta_0 + \pi$. Equation (33a) can be represented symbolically by a linear operator $\mathscr{L}$,

$$B_{n+1}(x) = \mathscr{L}[B_n(x)]. \tag{33b}$$

In the limit of $R_m \rightarrow \infty$ the magnetic field concentrates on a fractal set (Finn & Ott 1988; Du & Ott 1993). Thus we assume that the resulting time-asymptotic field is a generalized function which is an eigenfunction of (33). Formally, this is expressed as

$$\mathscr{L}[\tilde{B}(x)] = \lambda\tilde{B}(x), \tag{34}$$

where

$$\lambda = |\lambda|\,\mathrm{e}^{\mathrm{i}\phi}$$

is the complex eigenvalue corresponding to the generalized eigenfunction $\tilde{B}(x)$. The fast dynamo growth rate is then

$$\gamma_* = \frac{1}{T}\ln|\lambda|, \tag{35}$$

where T is the temporal period of the stretch–fold–slide flow, and instability corresponds to $|\lambda| > 1$. The angle ϕ specifies the fundamental frequency of oscillation, ϕ/T, for the eigenfunction.

4.2. *Check of the growth rate formula*

The advantage of the model $(33a)$ is that analytical calculations are relatively easy. To calculate λ, we consider the flux integral $\Phi_{n+1} = \int_0^1 B_{n+1}(x)\,\mathrm{d}x$. Using $(33a)$ for $B_{n+1}(x)$ we immediately obtain

$$\Phi_{n+1} = (1+\mathrm{e}^{\mathrm{i}\theta})\,\Phi_n. \tag{36}$$

Hence, identifying λ with the flux growth rate (Finn & Ott 1990), we have

$$\lambda = 1+\mathrm{e}^{\mathrm{i}\theta}, \tag{37}$$

which yields instability for $|1+\mathrm{e}^{\mathrm{i}\theta}| > 1$. (Note that $\phi = \arg(\lambda)$ is a function of θ; $\tan\phi = \sin\theta/(1+\cos\theta)$.)

In what follows we attempt to show that (35) and (37) for the growth rate satisfy the general formula (24). To this end we normalize the eigenfunction so that $\int_0^1 \tilde{B}(x)\,\mathrm{d}x = 1$, and we write the magnetic field at $z = 0$ and at the time n ($n \ll 1$) as

$$B(x,n) = \mathrm{Re}\,[B_n(x)] = \mathrm{Re}\,[\lambda^n B_0 \tilde{B}(x)], \tag{38}$$

where $B_0 = |B_0|\exp(\mathrm{i}\xi)$ is a complex constant, and the real part used to obtain the actual field $B(x,n)$ results from our use of the complex representation, (32). Substituting in (9), we define

$$\hat{\chi}(\epsilon, \xi) = \sum_j |\mathrm{Re}\,\{\mathrm{e}^{\mathrm{i}\xi}\mu(I_j)\}|, \tag{39}$$

where I_j denotes the jth interval of length ϵ, $\mu(I_j) = \int_{I_j} \tilde{B}(x)\,\mathrm{d}x$, and $\hat{\chi}(\epsilon, \xi)$ in (39) is $\chi(\epsilon)$ of (9) multiplied by the factor $|\mathrm{Re}\,\{\mathrm{e}^{\mathrm{i}\xi}\int_0^1 \tilde{B}(x)\,\mathrm{d}x\}|$. Making use of $\tilde{B}(x) = \lambda^{-1}\mathscr{L}[\tilde{B}(x)]$ and the specific form of $\mathscr{L}$ given by $(33a)$, we have from (39)

$$\chi(\epsilon, \xi) = |\lambda|^{-1}[\chi(\epsilon/\alpha, \xi-\phi) + \chi(\epsilon/\beta, \xi-\phi+\theta)]. \tag{40}$$

Expanding $\chi(\epsilon, \xi)$ in a Fourier series in ξ, we have

$$\chi(\epsilon, \xi) = \sum_m \chi_m(\epsilon)\,\mathrm{e}^{\mathrm{i}m\xi}, \tag{41}$$

which when substituted in (40) yields

$$|\lambda|\,\chi_m(\epsilon)\,\mathrm{e}^{\mathrm{i}m\phi} = \chi_m(\epsilon/\alpha) + \chi_m(\epsilon/\beta)\,\mathrm{e}^{\mathrm{i}m\theta}. \tag{42}$$

To solve (42), we assume solutions of the form $\chi_m(\epsilon) = K_m\,\epsilon^{-\kappa_m}$ (where K_m and κ_m can both be complex). Substituting this form in (42), we obtain an equation for the exponent κ_m,

$$|\lambda|\,\mathrm{e}^{\mathrm{i}m\phi} = \alpha^{\kappa_m} + \beta^{\kappa_m}\,\mathrm{e}^{\mathrm{i}m\theta}. \tag{43}$$

This equation, in general (i.e. barring special choices for θ), has an infinite number of complex roots. Let

$$\kappa_m = \kappa_m^{(r)} + \mathrm{i}\kappa_m^{(i)},$$

where $\kappa_m^{(r)}$ and $\kappa_m^{(i)}$ are real. Then

$$\epsilon^{-\kappa_m} = \epsilon^{-\kappa_m^{(r)}}\exp[\mathrm{i}\kappa_m^{(i)}\ln(1/\epsilon)].$$

Thus such a root corresponds to an increase of $\chi_m(\epsilon)$ with decreasing ϵ as $\epsilon^{-\kappa_m^{(r)}}$ modulating a sinusoidal oscillation in the variable $\ln(1/\epsilon)$ with a period $2\pi/\kappa_m^{(i)}$. As

$\epsilon \to 0$, the sum in (41) will be dominated by the root of (43) with the largest value of $\kappa_m^{(r)}$. Taking magnitudes of both sides of (43) and noting that $|a+b| \leqslant |a| + |b|$, we have

$$|\lambda| \leqslant \alpha^{\kappa_m^{(r)}} + \beta^{\kappa_m^{(r)}}. \qquad (44)$$

Since α and β are both less than one, (44) implies an upper bound on $\kappa_m^{(r)}$

$$\kappa_m^{(r)} \leqslant \bar{\kappa}, \qquad (45)$$

where $\bar{\kappa}$ is the unique real positive root of

$$|\lambda| = \alpha^{\bar{\kappa}} + \beta^{\bar{\kappa}}. \qquad (46a)$$

We now note that this upper bound is actually attained: setting $m = 0$, we see that (43) reduces to (46a). Thus $\bar{\kappa}$ is in fact the cancellation exponent κ,

$$|\lambda| = \alpha^{\kappa} + \beta^{\kappa}. \qquad (46b)$$

(Note that in the purely two-dimensional case $k\Delta_0 \equiv 0$, implying by (37) that $\lambda = 0$, which from (46b) yields $\kappa = \infty$.)

We now show that (46b) is precisely the result obtained from (24). To do this we note that, for the map (31) for any initial condition (x_0, y_0), at time nT,

$$L_1 = 1/L_3 = (1/\alpha)^r (1/\beta)^{n-r}, \qquad (47)$$

where r is the number of times the orbit of length n starting from (x_0, y_0) visits the region $x < \alpha$. (Note that $L_2 = 1$ (from (29), $\delta z_{n+1} = \delta z_n$, for $\delta x_n = \delta y_n = 0$).) The second equality in (47) results since, by figure 5, there is a stretching by the factor $(1/\alpha)$ each of the r times the orbit visits $x < \alpha$, and a stretching by the factor $(1/\beta)$ each of the $(n-r)$ times it visits $x > \alpha$. We now note the following result from Farmer *et al.* (1983). The area of initial conditions yielding orbits of length n that visit $x < \alpha$ for r times is

$$A_{r,n} = C_{n,r} \alpha^r \beta^{n-r},$$

where $C_{n,r} = n! / [(n-r)! \, r!]$ is the binomial coefficient. (Note that

$$\sum_{r=0}^{n} A_{r,n} = (\alpha + \beta)^n = 1,$$

as it should.) Thus

$$\langle L_1 L_3^{\kappa} \rangle = \langle L_1^{1-\kappa} \rangle = \sum_{r=0}^{n} A_{r,n} (\alpha^{-r} \beta^{-(n-r)})^{1-\kappa}$$

$$= \sum_r C_{n,r} \alpha^{\kappa r} \beta^{\kappa(n-r)} = (\alpha^{\kappa} + \beta^{\kappa})^n. \qquad (48)$$

Now, substituting (48) in (24), and identifying t with nT and $|\lambda|$ with $\exp(\gamma_* T)$, we immediately obtain (46b). Hence, we have verified (24) for this example.

4.3. *Numerical computations*

In the next section we will provide numerical tests for (24). These additional tests will be via numerical experiments, and these experiments are necessarily subject to the usual limitations imposed by finite computer resources. Thus it is useful to benchmark the accuracy and performance of the numerical methods to be used in the next section by applying them to an analytically soluble example. Figure 6 shows such calculations using the stretch–fold–slide model of (33a) with $\theta = 1.4$, $\alpha = 0.45$, $\beta = 0.55$, and an initial condition of $B_{n=0}(x) = 1$.
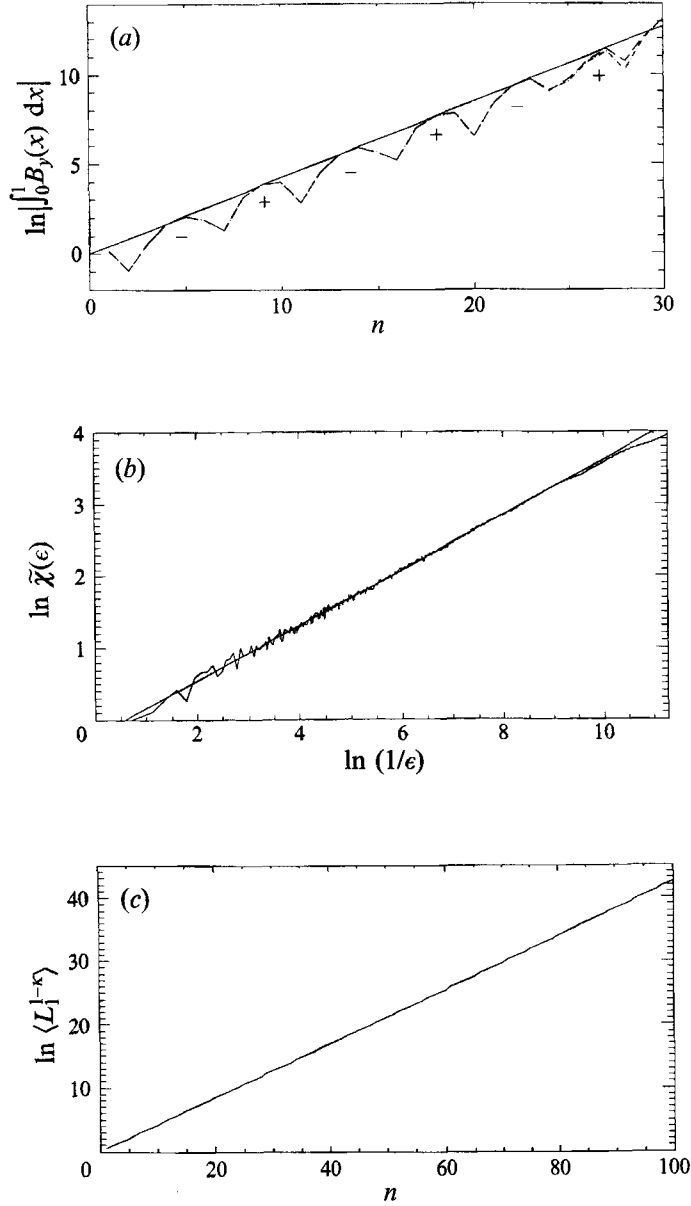
FIGURE 6. (a) $\ln|\int_0^1 B_y(x)\,dx|$ versus n. (b) $\ln\tilde{\chi}(\epsilon)$ versus $\ln(1/\epsilon)$ calculated at $n = 18$. (c) $\ln\langle L_1^{1-\kappa}\rangle$ versus n for $N_p = 10^5$. Superposed straight lines in (a) and (b) show the fits used to determine the numerical estimates quoted in the text. For all three plots, $\alpha = 0.45$, $\beta = 0.55$, $\theta = 1.4$ and the initial field in the $z = 0$ plane is one.

Figure 6(a) shows a plot of $\ln|\int_0^1 B_y(x,n)\,dx|$ versus n. Here $B_y(x,n)$ is calculated at $N_p = 10^8$ evenly spaced points $\{x_i\}$ in the interval $[0, 1]$, and the integral is approximated as $N_p^{-1}\sum_{i=1}^{N_p} B_y(x_i, n)$. Oscillations from positive values (indicated by $+$ in the figure) to negative values (indicated by $-$ in the figure) occur with a period in n of $2\pi/\phi$. The plot is done for two different grids (the dashed line and the dash dot line), i.e. one grid is shifted from the other grid by $\frac{1}{2}\epsilon$ where $\epsilon = 1/N_p = 10^{-8}$. For $n \leqslant 24$ the two plots are the same; after this time they diverge. This occurs because the magnetic field tends

to oscillate more wildly and to concentrate on a fractal as time increases; hence the number of points needed to accurately approximate the integral becomes larger as time increases. Past $n \approx 24$ we regard the results as not reliable. From the straight-line fit in the figure we obtain a flux growth rate of 0.42, as compared to the theoretical value of 0.426... from (37).

Figure 6(b) shows a plot of $\ln \tilde{\chi}(\epsilon)$ versus $\ln(1/\epsilon)$ using $N_p = 10^8$ points and the magnetic field at iterate number $n = 18$. The interval used is again $[0, 1]$. We see that at small ϵ (i.e. $\ln(1/\epsilon) \gtrsim 10$) the numerical plot begins to deviate from the fitted straight line as a result of ϵ approaching the smallest scale generated at $n = 18$. At large ϵ (i.e. $\ln(1/\epsilon) \lesssim 3$) there appear to be fluctuations which may be either statistical or due to κ_m roots of (43) with non-zero imaginary parts. In the intermediate scaling range, the data are very well fitted by a straight line whose slope yields $\kappa \approx 0.382$ as compared to 0.385 from (46b).

Figure 6(c) shows a numerical plot of $\ln \langle L_1^{1-\kappa} \rangle$ versus n, where the average is performed over $N_p = 10^5$ initial points evenly spaced in the interval $[0, 1]$. Over the time interval shown, the data are almost perfectly fitted by a straight line whose slope yields a growth rate of $\gamma_* = 0.424$, which agrees well with the theoretical value of 0.426....

Note that the difference between using $\langle L_1 L_3^\kappa \rangle$ and the individually averaged Lyapunov numbers in the combination $\langle L_1 \rangle \langle L_3 \rangle^\kappa$ becomes greater the more inhomogeneous the stretching is, and the results for the two are the same if the stretching is uniform (e.g. $\alpha = \beta = \frac{1}{2}$ in the example of this section). For example, in the case of figure 6 ($\alpha = 0.45$, $\beta = 0.55$) the difference between our growth rate given by (24) and that calculated using $\langle L_1 \rangle^{1-\kappa}$ in place of $\langle L_1^{1-\kappa} \rangle$ is only 1%; on the other hand, for $\alpha = 0.3$ and $\beta = 0.7$ this difference increases to about 15%, a difference that would be detected by our numerical calculations.

5. A temporally periodic flow

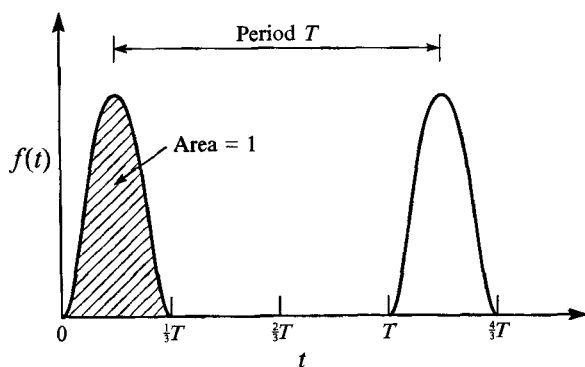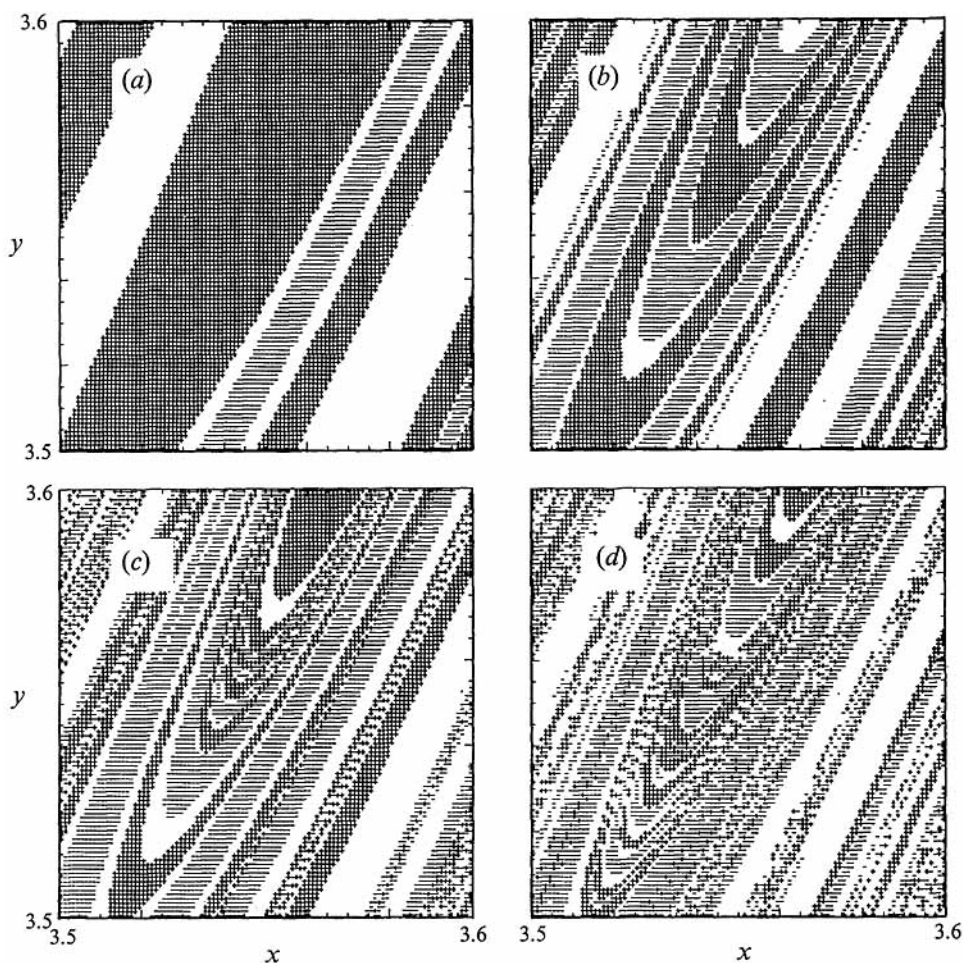### 5.1. *The model flow*

Consider an incompressible flow

$$v(x, t) = x_0 v_x(y, z) f(t) + y_0 v_y(z, x) f(t - T/3) + z_0 v_z(x, y) f(t - 2T/3), \qquad (49)$$

where $f(t)$ is periodic function with period T and $f(t) = 0$ for $T/3 + nT < t < (n+1)T$ (see figure 7) so that the flows in the x-, y- and z-directions are turned on separately. Also we assume that $f(t)$ is normalized so that $\int_0^T f(t) \, dt = \int_0^{T/3} f(t) \, dt = 1$. Integrating $dx/dt = v(x, t)$ through one period T, one obtains a volume-preserving map relating x at $t = nT$ to x at $t = (n+1)T$

$$\left. \begin{aligned} x_{n+1} &= x_n + v_x(y_n, z_n), \\ y_{n+1} &= y_n + v_y(z_n, x_{n+1}), \\ z_{n+1} &= z_n + v_z(x_{n+1}, y_{n+1}), \end{aligned} \right\} \qquad (50)$$

which is not dependent on the specific form of $f(t)$ (thus the fast dynamo problem will also be independent of the specific form of $f(t)$; see (5b)). Choosing v_x, v_y and v_z in the form

$$v_x = A \sin z + D \cos y,$$

$$v_y = B \sin x + E \cos z,$$

$$v_z = C \sin y + F \cos x,$$

FIGURE 7. Schematic plot of $f(t)$.

FIGURE 8. Locations of points on a 100×100 grid whose magnetic field contributes 90% of Φ' at (a) $n = 4$, (b) $n = 5$, (c) $n = 6$, and (d) $n = 7$. Points with positive and negative B_z are plotted as positive and minus signs, respectively.

the flow, (49), yields the map

$$\left.\begin{array}{l} x_{n+1} = x_n + A\sin z_n + D\cos y_n, \\ y_{n+1} = y_n + B\sin x_n + E\cos z_n, \\ z_{n+1} = z_n + C\sin y_{n+1} + F\cos x_{n+1}. \end{array}\right\} \tag{51}$$

(Note when $A = E$, $B = F$ and $C = D$, the map (51) becomes the so-called ABC map of Du & Ott (1993), Feingold, Piro & Kadanoff (1988) and Finn & Ott (1988).)

In the following subsection we present numerical results for this flow. For all the reported numerical results, the initial magnetic field (§5.2) is the z-direction with a uniform strength of one, and we choose $A = B = C = 0$, $D = 2.3$, $E = 2.5$ and $F = 2.7$. For these chosen parameters, the three Lyapunov numbers are $(0.74, 0.25, -0.99)$ and the chaotic region extends throughout almost all space, i.e. there are no sizeable KAM tori.

5.2. *Fast dynamo problem*

Let $B_n(x)$ denote the magnetic field at time $t = nT$. The evolution of $B_n(x)$ in the infinite-conductivity case is governed by (30) with $DM(x)$ the Jacobian matrix of the map transformation (51). Thus, to calculate B_n at any given point x, we first iterate the map (51) backward n steps to find the orbit leading to x at time n from an initial condition at time zero. We then iterate (30) forward along the above-determined orbit using the specified initial condition $B_{n=0}$.

Refer to figure 8(*a–d*) (similar figures are given in Du & Ott 1993). To explain the meaning of these figures we describe how they are produced. We first calculate the magnetic field on a 100×100 grid on the surface $S: 3.5 \leqslant (x, y) \leqslant 3.6$ and $z = 0$. We label the $N = 100 \times 100 = 10^4$ grid points with an index i ($1 \leqslant i \leqslant N$) according to the prescription that the component of the magnetic field normal to S at the grid point i, denoted by $B_{z,i}$, satisfies $|B_{z,i}| \geqslant |B_{z,i+1}|$. (That is, we arrange the $B_{z,i}$ in size order). We then estimate $\Phi' = \int_S |B_z| \, \mathrm{d}^2 x$ via

$$\Phi' \approx \sum_{i=1}^{N} |B_{z,i}| A/N,$$

where A is the area of S. Now, starting with the grid point with the largest value of $|B_{z,i}|$ (i.e. the smallest i), we successively mark positions on the grid until the plotted points account for 90 % of Φ'. That is, we mark the grid point with indices $1 \leqslant i \leqslant N_0$, where N_0 is the smallest integer satisfying

$$\sum_{i=1}^{N_0} |B_{z,i}| A/N \geqslant 0.90 \sum_{i=1}^{N} |B_{z,i}| A/N.$$

The points in figure 8 with positive B_z and with negative B_z are plotted as plus and minus signs, respectively. Figures 8(*a*)–8(*d*) refer to four successive times, $n = 4, 5, 6$ and 7. We clearly see from these figures that finer scale structure is generated with increasing time. Referring to figure 8(*d*) we also see that the magnetic field variation is apparently predominantly in the direction perpendicular to long thin bands in the figure. Along the direction of these bands the magnetic field is comparatively weakly varying. The observation that on a two-dimensional cross-section the magnetic field is weakly varying along curves indicates that the magnetic field is weakly varying on two-dimensional surfaces in the whole three-dimensional dynamo region. Thus we have verified that the generated magnetic field structure is sheet-like.

We now calculate the flux growth rate by a direct computation of the flux. Since the magnetic field is sheet-like, a line segment, instead of an area, will be sufficient. The
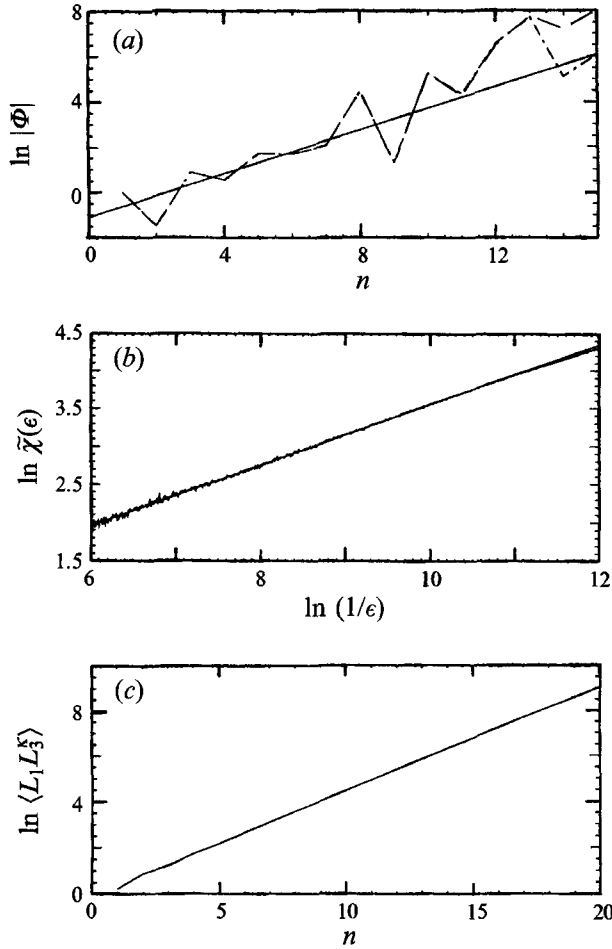
FIGURE 9. (*a*) $\ln|\Phi_z|$ versus *n*. The superposed straight line in (*a*) is a line of slope determined from (*c*). (*b*) $\ln\tilde{\chi}(\epsilon)$ versus $\ln(1/\epsilon)$ calculated at $n = 14$. The straight line shown is the fit to the data. (*c*) $\ln\langle L_1 L_3^\kappa\rangle$ versus *n* for $N_p = 10^6$.

chosen line segment has *y*- and *z*-coordinates $y = z = 1$ and has a length of 2π parallel to the *x*-axis. We calculate B_z at $N_p = 10^7$ evenly spaced points on the line segment to approximate the flux Φ as $\Sigma\, 2\pi B_z/N_p$. (We have also done computations with another line segment which gives a similar result.) Figure 9(*a*) shows plots of $\ln|\Phi|$ versus *n* for two different grids (the dashed line and the dash-dot line). In the range $n \lesssim 13$ the two results agree, showing that the data are reliable in this range. For $n \gtrsim 13$ the results using the two grids begin to diverge, indicating loss of sufficient resolution in the calculation.

Next, we calculate the cancellation exponent κ. We use the same line segment as in the previous paragraph and calculate the magnetic field on N_p evenly spaced points for time $n = 14$. We then calculate $\tilde{\chi}(\epsilon)$ and graph the plot of $\ln\tilde{\chi}(\epsilon)$ versus $\ln(1/\epsilon)$ as shown in figure 9(*b*). The straight line is the linear fit to the data and its slope yields $\kappa = 0.40$.

Finally, we calculate the average $\langle L_1 L_3^\kappa\rangle$ as a function of time using the method described at the end of §3. Figure 9(*c*) show a plot of $\ln\langle L_1 L_3^\kappa\rangle$ versus *n*, where the average is take on $N_p = 10^6$ initial points. The data are almost perfectly fitted by a

straight line, whose slope yields a growth rate of 0.48. We then fit the data in figure 9(a) up to $n \sim 13$ with a straight line of slope 0.48. The fit is shown as the solid line in figure 9(a). It can be seen that the line fits the data reasonably well.

6. Conclusion

This paper has developed a simple formula, (24), for the dissipationless limit (i.e. $R_m \to \infty$) of the growth rate of the fast kinematic dynamo instability. The growth rate is given in terms of the cancellation exponent and the infinite-time limit of an average of finite-time Lyapunov numbers of the chaotic flow. The quantities in the growth rate formula can all be obtained solely from consideration of the dissipationless dynamics. Thus we establish a connection between the ergodic stretching properties of the underlying chaotic flow and the instability growth (see also Aurell & Gilbert 1992; Finn & Ott 1990). Since the result is based on heuristic considerations, it has been checked against an analytically soluble example and numerical experiments, with good results. The numerical experiments also show that numerical calculations based on the growth rate formula are very feasible and converge well.

Appendix A. The case $\kappa > 1$

In the main body of this paper, we have discussed cases where $\kappa < 1$. When $\kappa > 1$, (24) implies that there is no exponential growth (and thus no dynamo action) for sheet-like magnetic field structure. However, in numerical calculations care must be taken when this is the case. In particular, our definition of κ given in §2 makes sense for $\kappa < 1$, but has to be modified to define κ so that the more singular case of $\kappa > 1$ makes sense.

From discussions in §2, we have

$$\sum_i \left| \int_{J_i} \boldsymbol{B}(\boldsymbol{x}, t) \, \mathrm{d}x \right| \sim 1/\epsilon^\kappa \quad \text{for} \quad \epsilon > \epsilon_*.$$

Here i denotes one of the ϵ-length intervals. Since the total number of ϵ-length intervals is of order $(1/\epsilon)$, the average of $|\int_i \boldsymbol{B}(\boldsymbol{x}, t) \, \mathrm{d}x|$ is given by

$$\left\langle \left| \int_i \boldsymbol{B}(\boldsymbol{x}, t) \, \mathrm{d}x \right| \right\rangle \sim \epsilon^{1-\kappa}. \tag{A 1}$$

Numerically, we calculate the magnetic field at a large number of evenly spaced points, and the integral in (A 1) is estimated as

$$\left| \int_i \boldsymbol{B}(\boldsymbol{x}, t) \, \mathrm{d}x \right| \approx \left| \varDelta \sum_{x_p \in I_i} \boldsymbol{B}(x_p, t) \right|, \tag{A 2}$$

where $\varDelta$ is the separation between two neighbouring points, x_p denotes the coordinates of one of the evenly spaced points, and I_i denotes the ith interval. For $\kappa > 1$, (A 1) then implies that the average of $|\int_i \boldsymbol{B}(\boldsymbol{x}, t) \, \mathrm{d}x|$ (or $|\sum_{x_p \in I_i} \boldsymbol{B}(x_p, t)|$) increases with decreasing
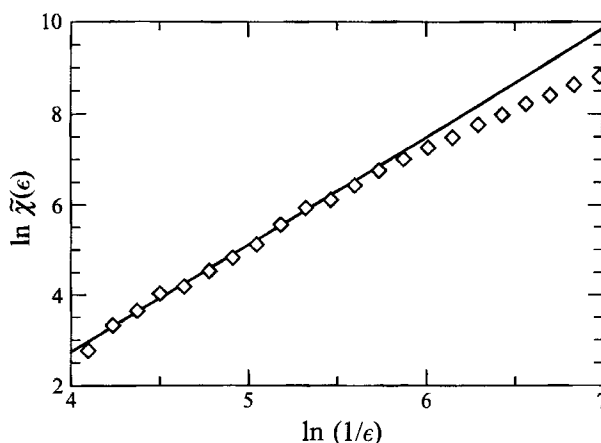
FIGURE 10. $\ln \tilde{\chi}(\epsilon)$ versus $\ln(1/\epsilon)$. The cutoff occurs near $\ln(1/\epsilon) = 6.0$ owing to our finite number of applications of the map ($n = 12$).

ϵ (even though the number of contributing points decreases) provided that $\epsilon > \epsilon_*$. Hence, for a single point x_p in I_i, we typically expect to find that

$$|B(x_p, t)| \Delta \gtrsim |\int_i B(x, t) \, dx|.$$

The estimate of $|\int_i B(x, t) \, dx|$ via (A 2) thus can depend strongly on whether a single bordering point is included in I_i or not. That is, the inclusion or exclusion of a single boundary point in the grid can make a large change in $|\int_i B \, dx|$. Thus, for $\kappa > 1$, computation of κ in this way does not make sense.

To remedy this, we introduce the following improved definition of κ. We first smooth the magnetic field over a range $\epsilon > \epsilon_*$,

$$B'(x, t, \epsilon) = \int B(x', t) \times \frac{1}{(2\pi)^{\frac{1}{2}} \epsilon} e^{-|x-x'|^2/(2\epsilon^2)} \, dx'. \tag{A 3}$$

(The result for κ is independent of the precise form of the smoothing (Gaussian for (A 3)).) Then we calculate $\chi(\epsilon)$ via

$$\chi(\epsilon) = \frac{\int |B'(x, t, \epsilon)| \, d^3x}{\left|\int_V B'(x, t, \epsilon) \, d^3x\right|}. \tag{A 4}$$

The cancellation exponent κ is then given by

$$\kappa = \lim_{\epsilon \to 0} \frac{\ln \chi(\epsilon)}{\ln(1/\epsilon)}. \tag{A 5}$$

Noting that $\chi(\epsilon)$ in (A 4) is essentially the left-hand side of (12) and that (A 5) implies the scaling on the right-hand side of (12) with ϵ_* replaced by ϵ, we see that our new definition for κ is consistent with the previous one. We have numerically verified for several examples that, as expected, this definition give the same result as the definition in §2 when $\kappa < 1$.

As an illustration we now use the model in §4 to test the modified definition of the cancellation exponent in the case $\kappa > 1$. We choose $\alpha = 0.45$, $\beta = 0.55$ and $\theta = 2.8$. From (46b), we obtain a theoretical prediction of $\kappa = 2.58$. In figure 10 we show our numerical plot of $\ln \chi(\epsilon)$ versus $\ln(1/\epsilon)$, in which each diamond represents one data
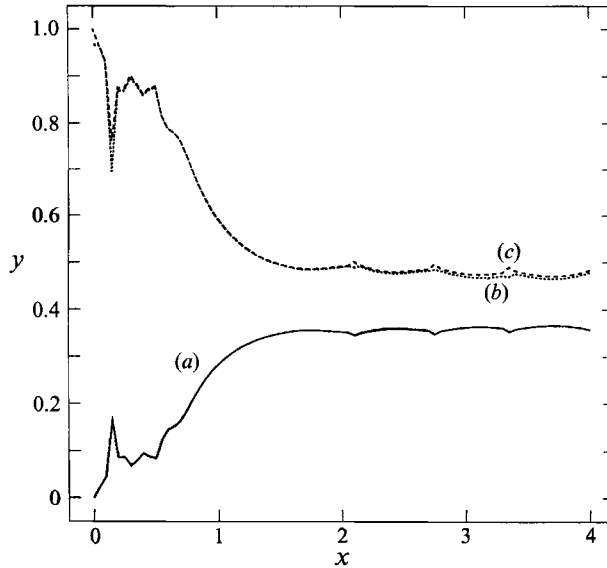
FIGURE 11. Dependence on the shear parameter α of (a) the growth rate $\gamma(\alpha)$, (b) the cancellation $\kappa(\alpha)$, and (c) the prediction of $\kappa(\alpha)$ from (B 3). This computation used $N = 1024$ cell. The jagged structure at small α is due to the discretization; the kinks at larger values of α correspond to mode crossings.

point and the solid line is the linear fit to the data. The slope of the linear fit yields an estimated value of $\kappa = 2.36$, which is in reasonable agreement with the result of (46 b). Numerical application of the definition in §2, on the other hand, yields $\kappa = 1$ in all cases where the theory predicts $\kappa > 1$.

Appendix B. Cancellation exponents of the stretch–fold–shear dynamo

By B. J. Bayly[1] and A. Rado[2]

[1] Mathematics Department, University of Arizona, Tucson, AZ 85721, USA
[2] Courant Institute of Mathematical Sciences, 251 Mercer Street, New York, NY 10012, USA

The stretch–fold–shear dynamo introduced by Bayly & Childress (1988) is a simple model akin to the Finn–Ott generalized baker's dynamos (Finn & Ott 1988) and the stretch–fold–slide model analyzed by Du and Ott in the foregoing paper. Because the shear is smoothly varying, the Bayly–Childress model cannot be solved exactly except in special cases. It is still easy to treat numerically, and represents an intermediate case between analytically solvable models and the extremely complex dynamos seen in chaotic three-dimensional flows. Stretch–fold–shear models have the nice feature that the shear parameter can be varied continuously. When Du and Ott first presented the idea of the cancellation exponent (Du & Ott 1993), we decided to find out how the cancellation exponent depends on the shear parameter, and see whether there was any connection between the cancellation exponent and the growth rate.

   The stretch–fold–shear dynamo (Bayly & Childress 1988) is described by the operator G:

$$[Gb](y) \equiv 2\exp\left(-2\pi i \alpha\left(y - \tfrac{1}{2}\right)\right)\begin{cases} b(2y) & \text{if } 0 < y < \tfrac{1}{2}; \\ -b(2-2y) & \text{if } \tfrac{1}{2} < y < 1. \end{cases} \qquad (B\ 1)$$
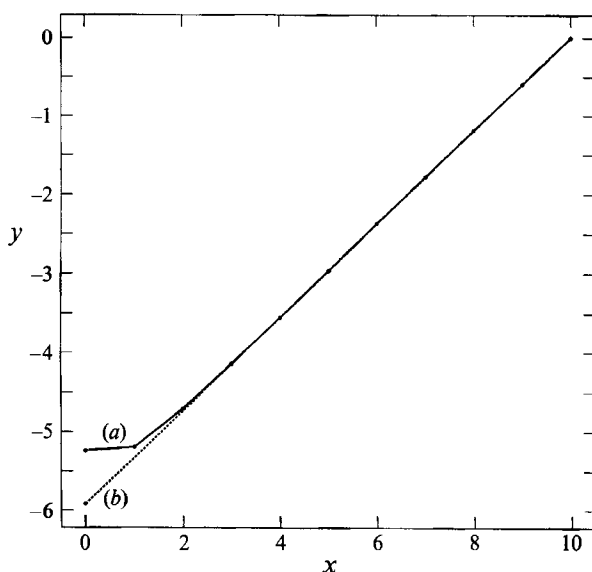
FIGURE 12. Calculation of cancellation exponents. Curve (*a*) (solid line) is a plot of $\log_2 \chi(\epsilon)$ as a function of $\log_2(1/\epsilon)$ for $\epsilon = 2^{-p}$, $p = 0, 1, ..., 10$. Curve (*b*) (dotted line) is the straight-line fit to the datapoints for $p = 3, 4, ..., 10$.

Here $b(y)$ is any complex scalar function defined on $0 < y < 1$, and α is the shear parameter. We discretize (B 1) by dividing the interval $(0, 1)$ into $N = 2^P$ equal subintervals and approximating $b(y)$ by a constant value in each subinterval. This yields a finite-dimensional matrix approximation to the operator G. The eigenvalue $\lambda(\alpha)$ of largest modulus and the corresponding eigenvector $\hat{b} \equiv (b_1, b_2, ..., b_N)$ can easily be found. The growth rate of the stretch–fold–shear dynamo is

$$\gamma(\alpha) = \log(|\lambda(\alpha)|). \tag{B 2}$$

Curve (*a*) in figure 11 shows the growth rate as a function of α.

The cancellation exponent $\kappa(\alpha)$ is computed using the dominant eigenvector $\hat{b}$ as the 'density' of the signed measure. Using $\epsilon = 2^{-p}$ for $p = 0$ to P yields graphs like figure 12 for $\log_2 \chi(\epsilon)$ versus $\log_2(1/\epsilon)$. The graphs we obtained are all fitted extremely well by straight lines, showing the existence of a robust cancellation exponent. Curve (*b*) in figure 11 shows the cancellation exponent κ as a function of α. It is plausible that a simple linear relation exists between the cancellation exponent and the growth rate. Du & Ott's theory predicts

$$\kappa(\alpha) = 1 - \gamma(\alpha)/\log(2). \tag{B 3}$$

Curve (*c*) in figure 11 shows this prediction, and the agreement with the direct computation is excellent.

REFERENCES

ARNOL'D, V. I., ZELDOVICH, YA. B., RUZMAIKIN, A. A. & SOKOLOV, D. D. 1981 *Sov. Phys. JETP* **81**, 2050.

AURELL, E. & GILBERT, A. D. 1992 Fast dynamos and determinants of singular integral operators. Preprint.

BAYLY, B. J. 1986 *Phys. Rev. Lett.* **57**, 2800.

BAYLY, B. J. & CHILDRESS, S. 1988 *Geophys. Astrophys. Fluid Dyn.* **44**, 211.

DU, Y. & OTT, E. 1993 Fractal dimensions of fast dynamo magnetic fields. *Physica* D (to appear).

FARMER, J. D., OTT, E. & YORKE, J. A. 1983 *Physica* D **7**, 153.

FEINGOLD, M., PIRO, O. & KADANOFF, L. P. 1988 *J. Statist. Phys.* **50**, 529.

FINN, J. M., HANSON, J. D., KAN, I. & OTT, E. 1991 *Phys. Fluids* B **3**, 1250.

FINN, J. M. & OTT, E. 1988 *Phys. Fluids* **31**, 2992.

FINN, J. M. & OTT, E. 1990 *Phys. Fluids* B **2**, 916.

GALLOWAY, D. & FRISCH, U. 1986 *Geophys. Astrophys. Fluid Dyn.* **36**, 53.

MOFFATT, H. K. & PROCTOR, M. R. E. 1985 *J. Fluid Mech.* **154**, 493.

OTT, E., DU, Y., SREENIVASAN, K. R., JUNEJA, A. & SURI, A. K. 1992 *Phy. Rev. Lett.* **69**, 2654.

SOWARD, A. M. 1987 *J. Fluid Mech.* **180**, 267.

VISHIK, M. M. 1989 *Geophys. Astrophys. Fluid Dyn.* **48**, 151.

YOMDIN, Y. 1987 *Israel J. Maths* **57**, 285.

ZEL'DOVICH, YA. B. & RUZMAIKIN, A. A. 1980 *Sov. Phys. JETP* **51**, 493.